Physics of Fluids

RESEARCH ARTICLE | JUNE 12 2023

Pressure amplification effect of initial compression waves in circumferential cracks of high-speed railway tunnel linings

Liu Yi-Kang (刘义康); Yang Wei-Chao (杨伟超); Deng E. (邓锷) ; Chen Zheng-Wei (陈争卫); Ni Yi-Qing (倪一清)

Physics of Fluids 35, 066119 (2023)
https://doi.org/10.1063/5.0155437

Physics of Fluids ARTICLE pubs.aip.org/aip/pof

Pressure amplification effect of initial compression waves in circumferential cracks of high-speed railway tunnel linings

Cite as: Phys. Fluids **35**, 066119 (2023); doi: 10.1063/5.0155437
Submitted: 20 April 2023 · Accepted: 25 May 2023 ·
Published Online: 12 June 2023

Yi-Kang Liu (刘义康),[1] Wei-Chao Yang (杨伟超),[1,2] E. Deng (邓锷),[3,4,a)] Zheng-Wei Chen (陈争卫),[3,4] and Yi-Qing Ni (倪一清)[3,4]

AFFILIATIONS

[1]School of Civil Engineering, Central South University, Changsha, China
[2]National Engineering Research Center of High-speed Railway Construction Technology, Changsha, China
[3]National Rail Transit Electrification and Automation Engineering Technology Research Center (Hong Kong Branch), Hong Kong, China
[4]Department of Civil and Environmental Engineering, The Hong Kong Polytechnic University, Hong Kong, China

[a)]**Author to whom correspondence should be addressed:** early.deng@polyu.edu.hk

ABSTRACT

Spalling of concrete blocks from tunnel linings is a severe defect in high-speed railway tunnels (HSRTs). The amplified initial compression wave (ICW) in circumferential cracks induced by high-speed trains may be the main cause of crack propagation and concrete block formation. To investigate the aerodynamic amplification effect of the ICW in circumferential cracks, tunnel-crack models are established and solved based on the unsteady viscous k–ε turbulence method. A scaled indoor experiment is carried out to verify the reliability of the calculation method. The characteristics of amplified pressure and corresponding mechanisms are analyzed and revealed. Three influential parameters, including the crack width, crack depth, and train velocity, are analyzed and discussed in detail. The main conclusions are as follows: (1) the maximum amplified pressure in a typical circumferential crack is 5.68 times that of the ICW. (2) The maximum power spectrum density (PSD) of the aerodynamic pressure at the crack tip is 91.04 times that at the crack mouth. The crack tip suffers most from the aerodynamic impact of the fluctuating component of pressure waves, whereas the crack mouth is most susceptible to the average component. (3) The train velocity is the most influential parameter on the maximum pressure at the crack tip, followed by the crack depth. The power function with an exponent of 2.3087 is applicable for evaluating the relationship between the maximum pressure and train velocities. (4) The train velocity and crack depth are most influential parameters to the maximum PSD. The relationship between the maximum PSD and the crack widths, crack depths, and train velocities can be reasonably described by the power function. (5) The mechanism of pressure amplification is as follows: first, the superposition of the internal energy possessed by air molecules near crack surfaces. Second, the increase in the internal energy of air near the crack tip because of the gradually narrowing space. The results of our research may be applicable in analyzing the cracking behavior of tunnel lining cracks and preventing the spalling of concrete blocks in HSRTs.

I. INTRODUCTION

Spalling of concrete blocks from tunnel linings is a severe defect in high-speed railway tunnels, which may cause train delays, train body damages, and even derailments.[1,2] Figure 1(a) shows a photo of spalling concrete blocks in a high-speed railway tunnel (HSRT). The complex aerodynamic pressure generated by moving high-speed trains is deemed to be a primary cause of concrete spalling.[3] When a train runs into an HSRT swiftly, an initial compression wave (ICW) arises due to the piston effect.[4–6] The ICW may amplify in lining cracks after it propagates into it. Consequently, stress concentration happens at the crack tip, leading to the propagation of lining cracks and the formation of spalling concrete blocks.[7]

In HSRTs, lining cracks are classified into three categories according to the angle between the crack and the longitudinal axis of the tunnel, namely, longitudinal cracks, circumferential cracks, and diagonal cracks. The circumferential crack is the most common type of crack in tunnels, as shown in Fig. 1(b). In a previous field survey in 13 tunnels, 1422 (53%) circumferential cracks are detected among

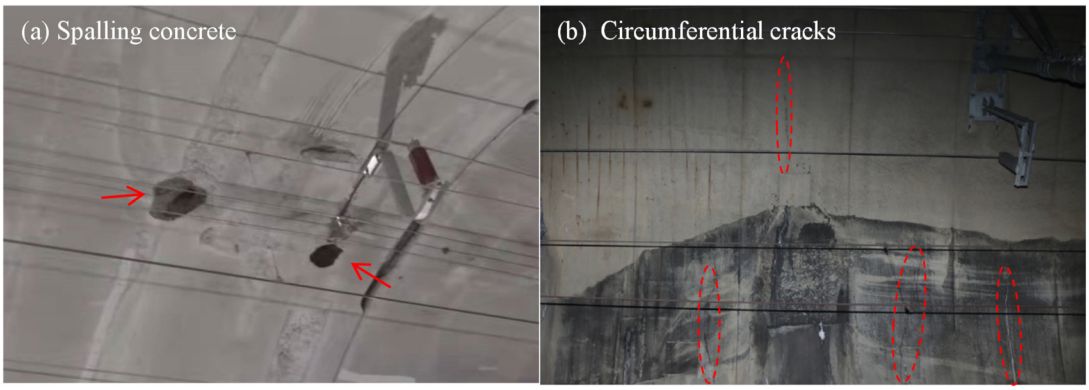

FIG. 1. Photos of (a) spalling concrete blocks and (b) circumferential cracks.

2683 lining cracks.[8] Therefore, it is essential to investigate the pressure amplification effect of ICW in circumferential cracks before assessing the probability of cracks propagating or deteriorating into concrete spalling.

Extensive studies were performed in the field of aerodynamic effects in HSRTs, in which the environmental consequences of aerodynamic pressure are most emphasized in recent years. Micro-pressure wave (MPW) produces when the aerodynamic pressure discharges from the tunnel exit, which generates strong plosive noises in the neighboring environment and induces vibrations to surround buildings. Researchers investigated this problem based on theoretical, experimental, and numerical methods.[9,10] For example, Baron *et al.*[11] introduced the classical linear acoustic formulation to predict the MPW. Zhang *et al.*[12] conducted moving model tests to compare the mitigation performance of five types of tunnel portals on the MPW. Okubo *et al.*[13,14] carried out field experiments to investigate the alleviation effect of bench shafts and tunnel hoods with windows on the MPW. Additionally, studies have also shown that the aerodynamic pressure may impair passengers' comfort and cause unwished train vibrations and damage. Passengers may experience dizziness and tinnitus when the aerodynamic pressure in an HSRT transmit into a train carriage.[15,16] As reported by Liu *et al.*,[17] compared with running in the open air, the vertical and horizontal vibration acceleration of a train increases by 47.2% and 33.8% when another train passes it in a tunnel due to the aerodynamic load. Based on the Carten–Dolan rule and Miner's rule, Zhou *et al.*[18] proved that the aerodynamic pressure in HSRTs contributes to a 25% decrease in the total fatigue life of matrix metals and welding joints of high-speed trains approximately. Considering that the strength of concrete is substantially lower than the metal of a train, it is intuitive to understand that the tunnel lining is more susceptible to aerodynamic impacts.

Few studies investigated the aerodynamic pressure-induced damage of tunnel linings. Based on Miner's theory, Gong and Zhu[19] performed a fatigue life estimation of tunnel lining under aerodynamic pressures. Using an equal-damage nonlinear model, Du *et al.*[20] also calculated the fatigue behavior of tunnel secondary lining considering the nonlinearity of aerodynamic effects caused by high-speed trains. Li *et al.*[21] investigated the fatigue damage characteristic of segmental linings of shield tunnels under cyclic aerodynamic loads based on the S-N curve of concrete. However, the above research mainly considers undamaged tunnel linings from the perspective of fatigue theory. Regarding tunnel linings with cracks, studies were mostly performed based on fracture mechanics. For instance, Wang *et al.*[22] simulated the random fracture behavior of tunnel linings with initial cracks. Xu and Ma[23] analyzed the stress intensity factor of tunnel lining cracks under train vibrations. Feng *et al.*[24] investigated the propagation process of tunnel cracks subjected to long-term train seismic loads. As revealed by the literature, however, the fracture performance of tunnel lining with cracks under aerodynamic pressures has not been reported. The necessity is evident to understand the ICW-induced aerodynamic pressure in circumferential cracks before we can analyze the corresponding cracking behavior.

The main contribution of our research is that we analyzed the aerodynamic amplification effect of the ICW in circumferential cracks and reveal the corresponding mechanism based on the unsteady viscous k–ε turbulence model. In Sec. II, the calculation strategy is introduced and a scaled experiment is performed to verify the reliability of the calculation method. In Sec. III, the characteristics of the pressure field and the corresponding power spectrum density are first investigated. Furthermore, the mechanism of pressure wave incidence and amplification in the circumferential crack is also revealed. In Sec. IV, the effect of three key factors, including the crack width, crack depth, and train velocity, on the characteristics of the amplified pressure are discussed in detail.

II. EVOLUTION OF ICW IN HSRT

Before investigating the pressure field in circumferential cracks, a preliminary analysis on the characteristic of the ICW in the HSRT is conducted. A full-scale moving mesh model for calculating the ICW is first established. As shown in Fig. 2, the HSRT has a standard horseshoe cross-sectional applied in China. The tunnel length, cross-sectional area, height, and maximum width of the HSRT are 3000 m, 100 m^2, 12.6, and 9.08 m. The atmosphere at two ends of the tunnel is simulated by two cuboids with length, width, and height of 250, 200, and 100 m. The nose tip of the high-speed train is placed 130 m away from the tunnel portal at the initial state. The CRH380B train with a cross-sectional area of $A_{train} = 11.29$ m^2 is chosen as representatives for calculation. The train model has eight carriages and the total length

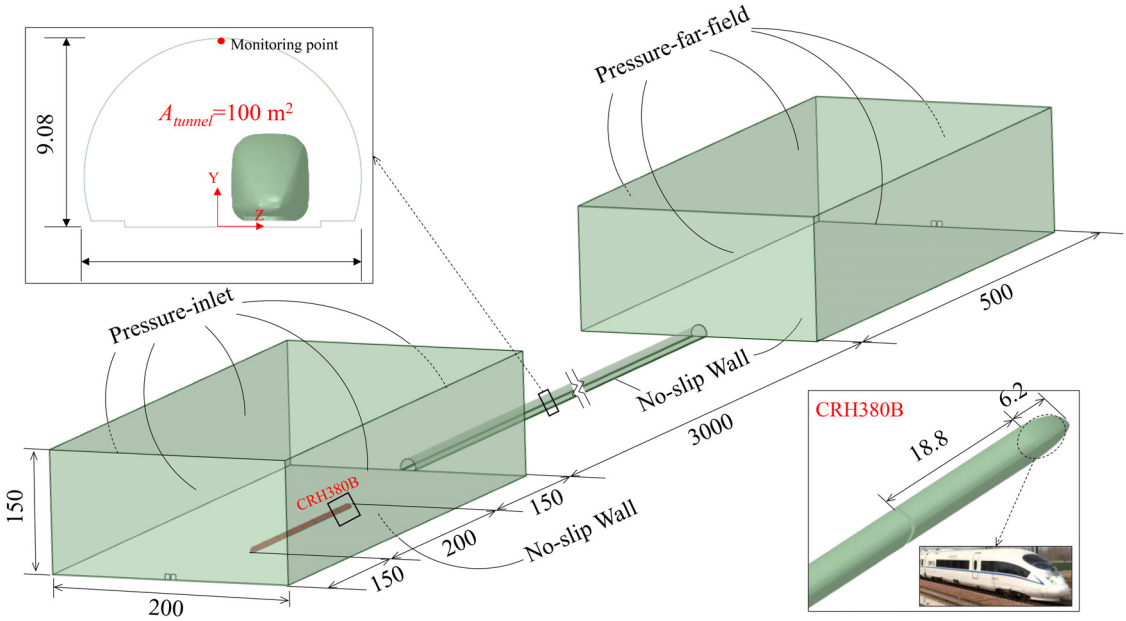

FIG. 2. Geometry of the moving mesh model (unit: m).

is 200 m. The width and height of the train is 3.3 and 3.9 m. The streamline length of the head carriage is 6.18 m. No-slip walls are assigned to the tunnel lining, ground, and train surfaces. The pressure far-field is applied to simulate other boundaries of the two cuboids. Five monitoring points are arranged at 500, 1000, 1500, 2000, and 2500 m along the longitudinal direction on the tunnel vault.

Figure 3 shows the grid distribution of the moving mesh model. As shown in this figure, the geometry model is meshed by polyhedral and hexahedron elements based on the "Mosaic" technology. The grid model is divided into moving grid area and static grid area, and Interface is utilized to convey flow field information between two areas. The train is operating in the moving grid area. For accuracy, the minimum grid size of the lining surface is 2 mm. Ten layers of prism grids are adhered to the train surface with a minimum height of 1.5 mm and a stretch ratio of 1.2. The total grid number of the moving mesh model is approximately 39 $\times$ 10^6.

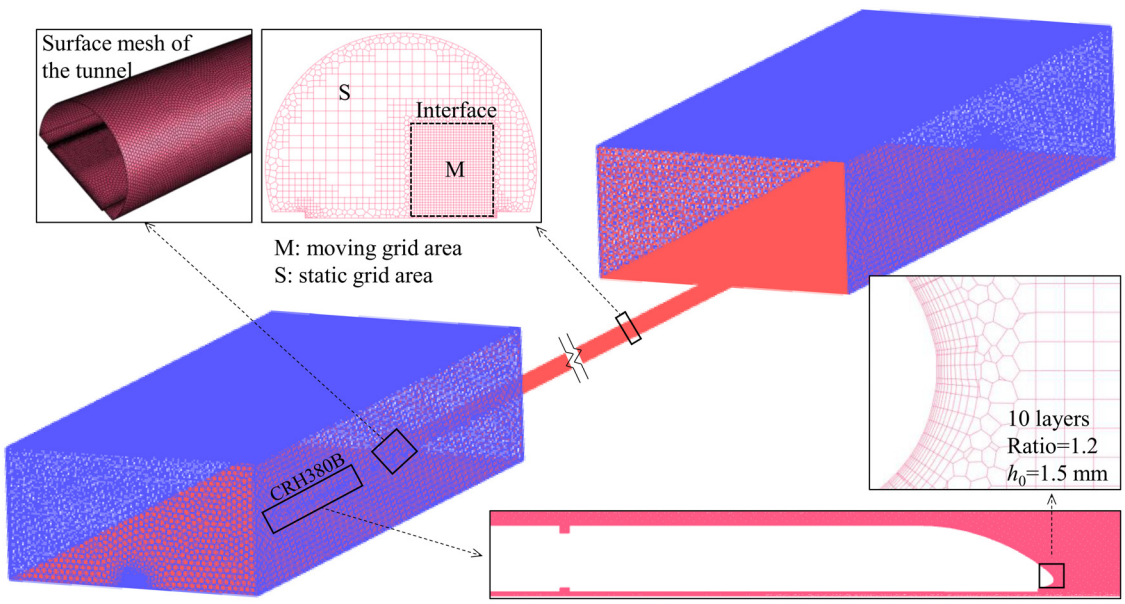

FIG. 3. Grid distribution of the moving mesh model.

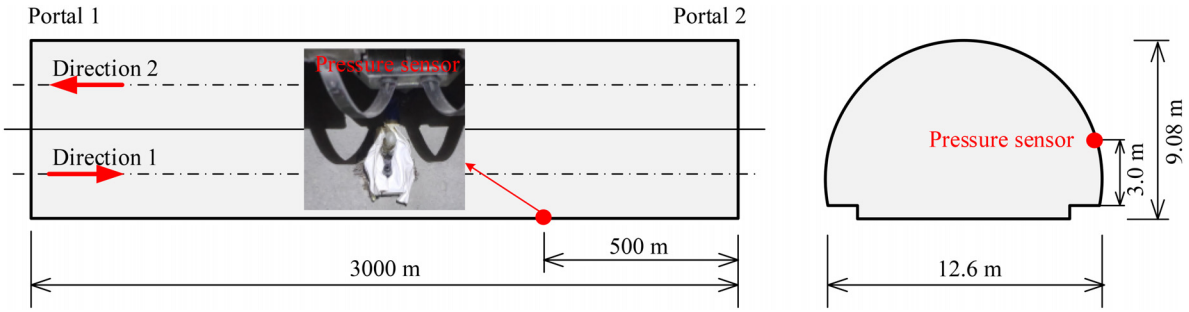

FIG. 4. Validation of the moving mesh model.

It is well known that the flow field around the train in tunnels is highly unsteady and turbulent. The piston effect and wave propagation in tunnels contributes a Reynolds number of over 10^6.[25,26] Moreover, the air is considered to be compressible flow when the Mach number is higher than 0.3. Although the Mach number is slightly lower than 0.3 in some cases involved in this research, the air flow is restricted in tunnels and the air compressibility should be taken into consideration. Otherwise, accurate pressure results cannot be calculated.[27] Considering these reasons, the compressible, unsteady, and viscous RNG k–ε turbulence model is adopted in this study. This turbulence model was successfully applied to solve complex train-tunnel aerodynamics.[25,26] The pressure-based solver with the SIMPLE algorithm is employed for the pressure-velocity coupling. The gradient is discretized based on the least squares cell method. The second-order upwind scheme is adopted for spatial discretization. The time step is 0.001 s. The residual and number of iterations for every step are 10^{-6} and 50, respectively.

The pressure data measured in a full-scale test are used to verify the moving mesh model. As shown in Fig. 4, the tunnel length is 3000 m, which corresponds to the length of the moving mesh model. The train type is CRH380B, and the train speed is 300 km/h. During the full-scale test, a pressure sensor (Honeywell DC030NDC4) is mounted 3 m high and 500 m away from Portal 2 on the tunnel lining surface. Detailed information about this type of pressure sensor can be found in.[28] A simulation is performed using the moving mesh model, and the results are then compared with the pressure data obtained from the full-scale test. As illustrated in Fig. 5, the pressure waveforms monitored in both the test and simulation exhibit strong agreement. Although minor discrepancies can be observed in the pressure curves, these could be attributed to different environmental factors such as air humidity and temperature, which can influence the wave speed. Nevertheless, the maximum pressure simulated by the moving mesh model has an error of only 4.4% and 3.0% when the train runs in directions 1 and 2, respectively. Hence, the moving mesh model demonstrates sufficient reliability for further computations.

Figure 6 shows the monitoring results the ICW. As shown in Fig. 6, an ICW is generated due to the instant entry of the train into the HSRT. When the ICW propagates longitudinally, the pressure of monitoring points rises orderly. The shape of pressure curves of monitoring points at different longitudinal positions is similar. The maximum pressure of different monitoring points is also close. However, the pressure curve is gradually steepening with the propagation distance increases. The maximum pressure gradient at 2500 m increases by 50.5% compared with that at 500 m. Similar phenomenon was also

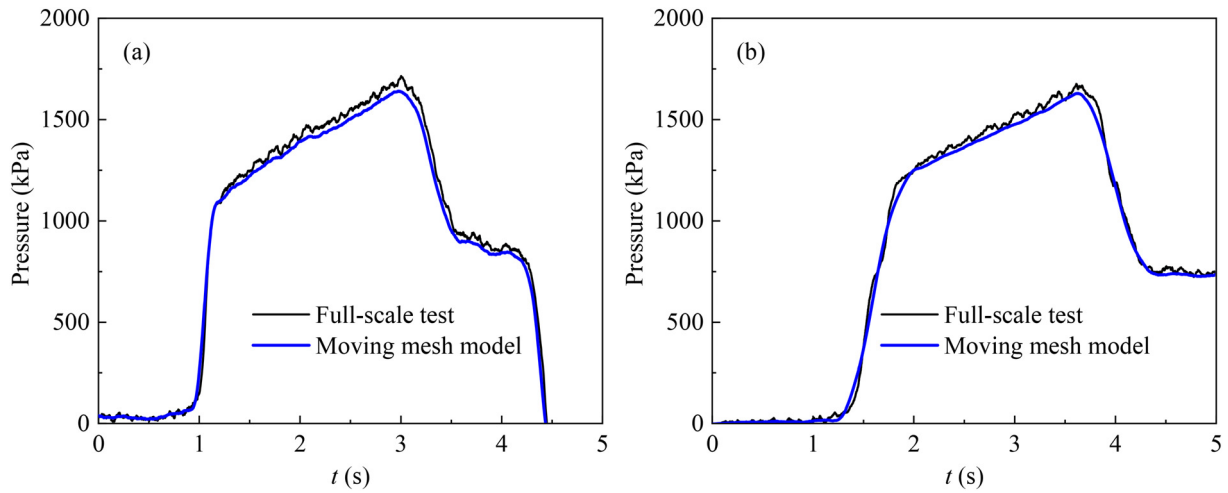

FIG. 5. Validation of the moving mesh model: (a) the train runs in direction 1 and (b) the train runs in direction 2.

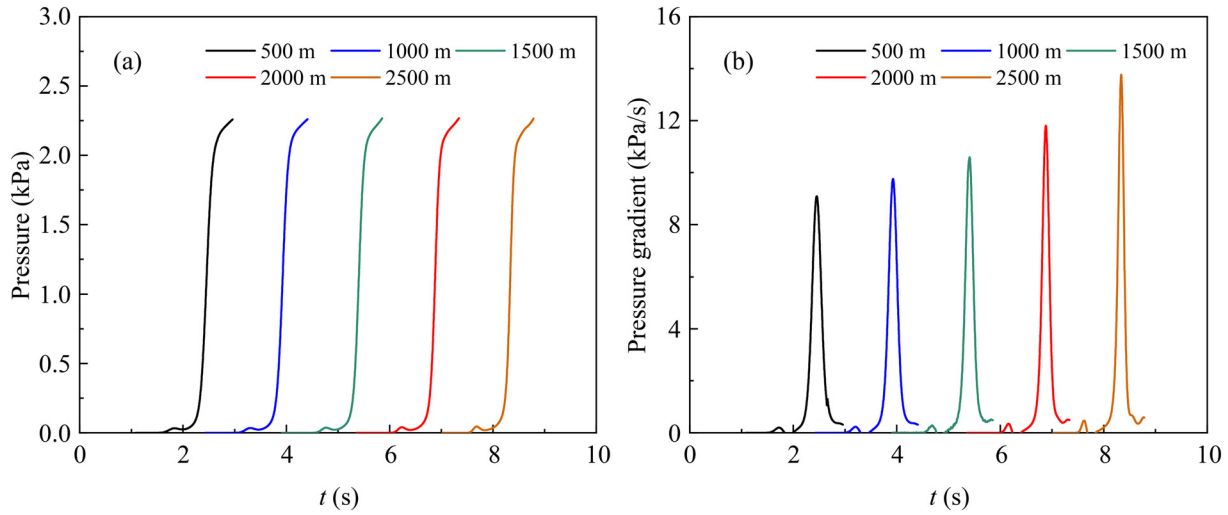

FIG. 6. The ICW in the HSRT: (a) pressure and (b) pressure gradient.

reported by previous study.[7,29] The reason is following: The temperature and air density increases when the air is compressed, resulting in the sound speed in the compressed air increases. Correspondingly, the wavefront steepens and the pressure gradient of the ICW increases.

III. CALCULATION STRATEGY

A. Establishment of CFD models

Tiny time steps must be used for calculating the aerodynamic pressure inside cracks because the size of the tunnel is hundreds of times that of the crack. The computational cost is unacceptable when using moving mesh models for calculating. Hence, a tunnel model with a length of 10 m is used to replace the full-length tunnel. This simplification is reasonable because the ICW is a typical plane wave propagating along the tunnel longitudinally. Reducing the tunnel length does not change the characteristic of a plane wave. The diagram of the tunnel lining with a circumferential crack is shown in Fig. 7. As shown in Fig. 7(a), three types of boundary conditions, including pressure-inlet, pressure-far-field, and no-slip wall, are employed in this model. The ICW is input from the pressure-inlet boundary in the form of plane wave. The turbulence intensity adopted on the pressure-inlet boundary is 1%. The pressure far-field is applied to simulate the longitudinally extended tunnel. No-slip walls are assigned to the tunnel lining, ground, and crack surfaces. Figure 7(c) presents the 3D view of the crack, respectively. The crack length is 100 mm in consideration of the size of spalling concrete blocks is greater than 100 mm.[2] The crack depth and width are 10–50 mm and 3–7 mm according to the statistical data in a Chinese standard Q/CR-405.2–2019[30] and a previous study.[7] The crack front is idealized as a semi-ellipse, a common practice in fracture analyses.[31] For convenience, all cases are named using symbols and numbers, where D is the crack depth, W is the crack width, and V is the train speed. The crack tip is symbolled as S. For instance, "D50-W4-V350" means that the crack depth is 50 mm, the crack width is 4 mm, and the train speed is 350 km/h. As shown in Fig. 8, eight monitoring points, named after "A" and "B," are arranged on two surfaces of the crack. Nine monitoring points, numbered orderly after "M," are placed on the middle plane of two crack surfaces along the crack depth and length directions.

The geometry model is also meshed by polyhedral and hexahedron elements. The element model of the crack D50-W5-V350 is shown in Fig. 9. As shown in this Figure, gradually changed sizes are assigned to all elements. Small-sized elements are applied to the space near the crack. Five layers of hexahedral elements with heights of 0.04 mm are assigned to the crack surfaces. Each model has a total element number of approximately 50 million. The calculation is also

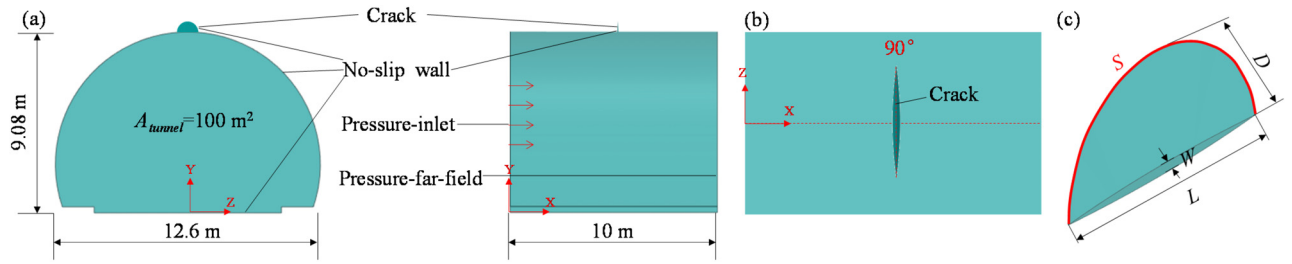

FIG. 7. Geometry model: (a) tunnel model; (b) top view; and (c) 3D view of the crack.

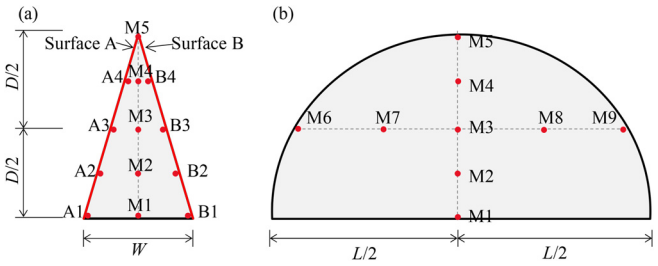

FIG. 8. Monitoring point arrangement: (a) the plane at *L*/2 and (b) the middle plane between two crack surfaces.

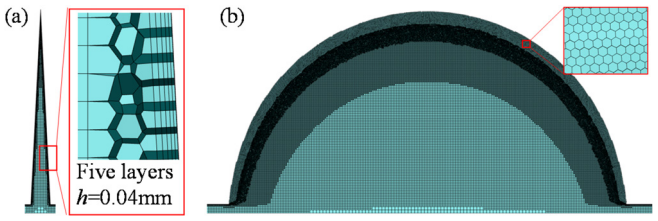

FIG. 9. Element model of the crack: (a) the plane at *L*/2 and (b) the middle plane between two crack surfaces.

performed using the unsteady viscous k–ε turbulence model. The SIMPLE algorithm, least squares cell method, and second-order upwind scheme are also adopted in the calculation. The physical time step is 5×10^{-8} s. The residual and number of iterations for every step are 10^{-6} and 50, respectively. The calculation for each model is approximately 34 days when using a supercomputer with a 4-node and 128-thread CPU.

According to the analysis in Sec. II, the pressure gradient of the ICW can approximate to infinite when the ICW transmits to a critical distance. Preliminary analyses also show that the pressure amplification lasts for a very short time. For the two reasons, the ICW is simplified as a constant pressure wave with pressure gradients of approximating to infinite. The maximum pressure of the simplified ICW is calculated using the moving mesh model established in Sec. II. For the train speed of 350 km/h, the ICW exerted onto the pressure-inlet boundary is shown in Fig. 10(b).

B. Sensitivity test

A sensitivity test of the element size is performed first for all models. The same mesh structure is generated base on the "Mosaic" meshing method when the element size varies. Namely, near the crack surface, the calculation domain is meshed by layered hexahedral grids near the crack surfaces, polyhedral transition grids, and core hexahedral grids. As shown in Fig. 10(a), five different element sizes, h of layered hexahedral elements ranges from 0.02 to 0.10 mm, are

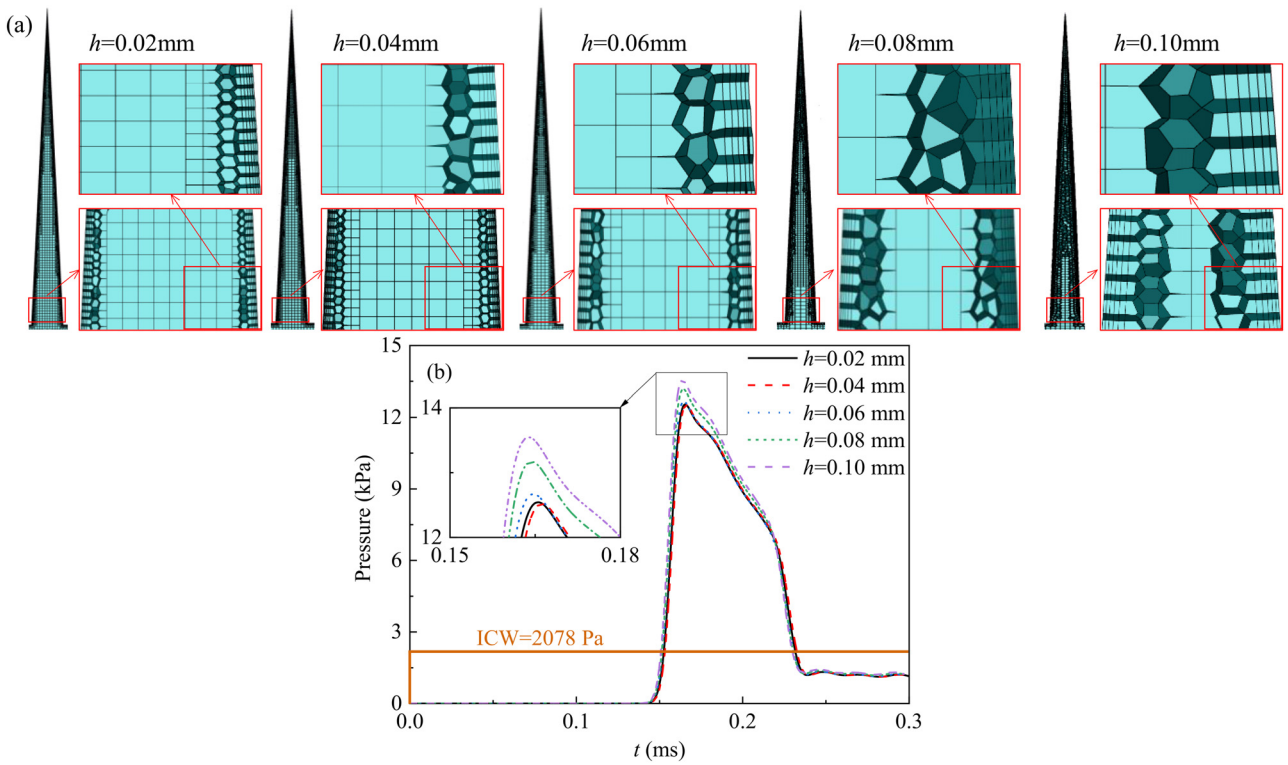

FIG. 10. Sensitivity test of element size: (a) different element sizes and (b) pressure results.

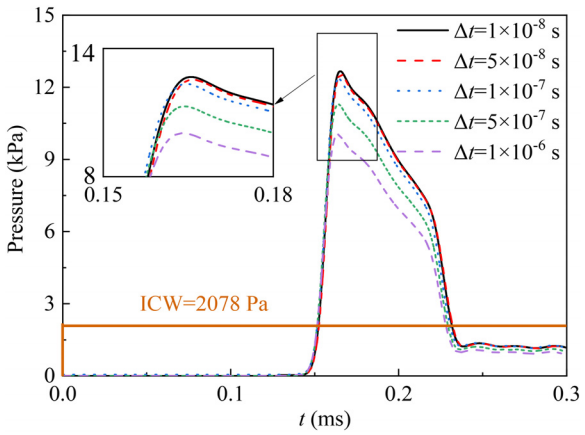

FIG. 11. Sensitivity test of time step.

considered. The pressure of M5 of the case D50-W5-V350 is presented here as an example. As shown in Fig. 10(b), the pressure time histories of models with different element sizes share the same change rule. The maximum pressure is affected by the element size. As plotted in the zoomed window, the maximum pressure obtained by models with h over 0.06 mm largely varies from those by models with higher element resolutions. When h is lower than 0.04 mm, the maximum pressure tends to converge to a fixed value, indicating that choosing the minimum element size of 0.04 mm ($y+ \approx 50$) is enough to avoid the element size-induced error.

To estimate the degree of convergence of pressure results caused by different time steps (Δt), various time steps, in the range of 1×10^{-8}–1×10^{-6} s, are adopted in the CFD calculation. As shown in Fig. 11, the time step size has an obvious influence on the simulated pressure results. When the time step is lower than 5×10^{-8} s, the maximum pressure tends to a constant value. The larger the time step is, the larger the deviation is. The difference between the maximum pressure obtained by models with time steps of 5×10^{-8} and 1×10^{-8} s is less than 1%. Hence, using a time step of 5×10^{-8} s is reasonable in CFD simulations.

C. Validation of CFD models

To verify the reliability of the CFD method in the present study, an indoor scaled experiment is carried out in this section. As shown in Fig. 12(a), the experimental model is fabricated by polyvinyl chloride material. The thickness of the transparent plate is 3 mm, which is thick enough to resist the deformation caused by the pressure. Figure 12(b) shows the internal cavity of the model. A crack with width, length, and depth of 5, 50, and 50 mm is connected with a cubic with a length of 50 mm. A hole with a diameter of 8 mm is drilled on one side to force a pressure of 3000 Pa by an air compressor. Five pressure monitoring holes, with diameters of 2.0 mm, are drilled on one side of the crack along the crack depth direction. As shown in Fig. 12(c), the CYY4 pressure sensor provided by the Xi'an Hangdong company is adopted to measure the pressure. The sampling frequency, pressure range, and precision are 50 kHz, ±5 kPa, and ±0.15%, respectively. A NI cDAQ-9188 CompactDAQ Ethernet Chassis is adopted to collect the pressure data obtained by five pressure sensors, as shown in Fig. 12(d). According to the geometry of the experimental model, a numerical model is established as shown in Fig. 13(a). The corresponding grid model is presented in Fig. 13(b). The calculation strategy and meshing method are consistent with those mentioned in Sec. III A. The input pressure and monitoring points of the numerical are consistent with the experiment.

Figure 14(a) compares the pressure results of V5 in the experiment and simulation. As shown in Fig. 14(a), when a pressure is input into the model, the pressure amplification happens in the crack. The pressure of the monitoring point V5 oscillates near 3000 Pa. The numerical model can replicate the pressure amplification and oscillation captured in the experiment. It is found that the pressure attenuation in the experiment is faster than in the simulation. The reason may be that the roughness of the experiment model is slightly higher than that of the simulation model. In addition, modifying the turbulence length scale of pressure-inlet boundary can be a solution to suppress excessive pressure oscillations. However, considering that our main

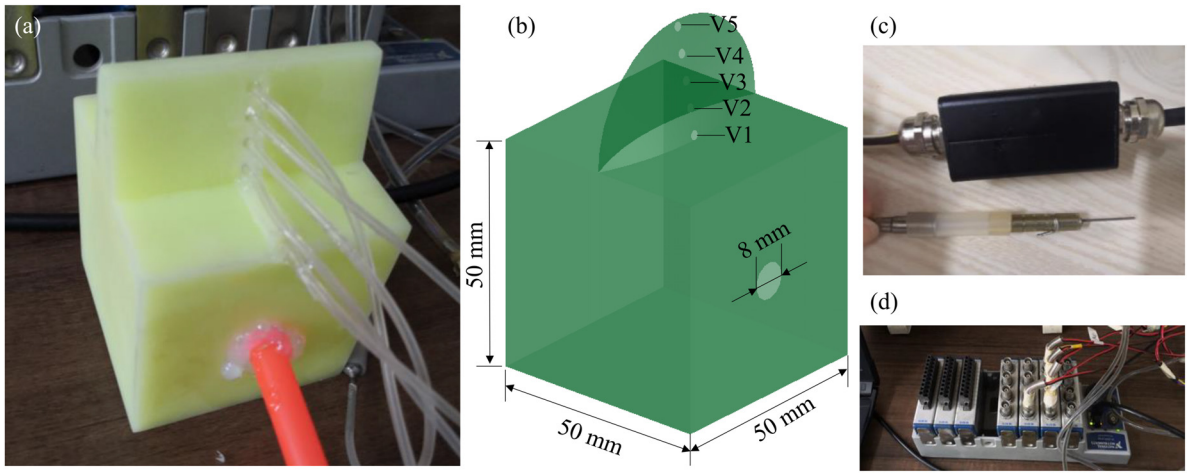

FIG. 12. Experiment setup: (a) model overview; (b) internal cavity; (c) pressure sensor; and (d) CompactDAQ Ethernet Chassis.

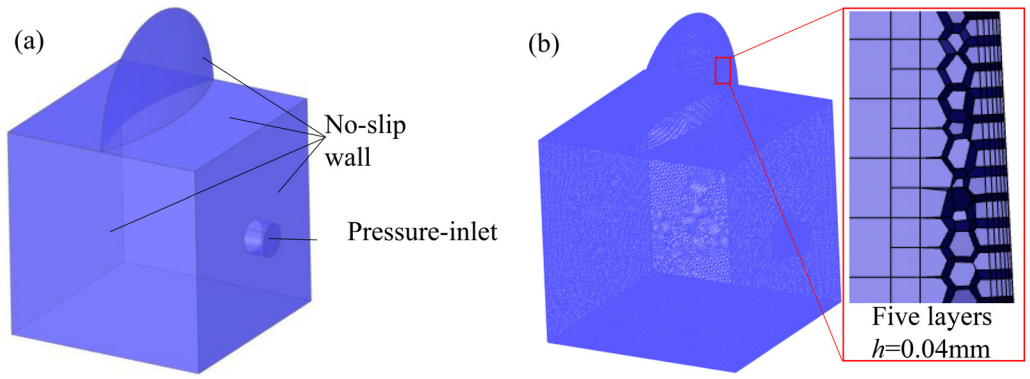

FIG. 13. Numerical model of the scaled experiment: (a) geometry model and (b) element model.

research interest is the pressure amplification effect, namely, the relative value of maximum amplified pressure in the crack to that of the initial compression wave, Fig. 14(b) further compares the maximum pressure obtained in the experiment and simulation. As illustrated in Fig. 14(a), the maximum pressure obtained in the experiment increases with the depth. This phenomenon is also captured by the numerical model. The maximum difference between the maximum pressure of the experiment and simulation is only 5.24%, indicating that the numerical method adopted in our study is reliable enough for further investigations.

IV. CHARACTERISTICS OF AMPLIFIED PRESSURE

A. Pressure field

Figure 15 shows the pressure time histories of monitoring points of *D*50-*W*5-*V*350. The zero data of the pressure time histories are not plotted in this figure as shown in Fig. 15.

The pressure in lining cracks is periodic waves with diminishing peaks. The pressure of each monitoring points oscillates for approximately five periods, and the shape of different periods is slightly different. The pressure peak of M5 decreases from 11.86 to 5.35 kPa in five periods, and the value of M3 decreases from 7.35 to 3.96 kPa, correspondingly. Negative pressures can be also observed in pressure time histories. However, the positive pressure peak of all monitoring points is substantially larger than the negative pressure peaks. The negative pressure peak of M5 is only −1.81 kPa at 0.44 ms.

Along the crack depth direction, the deeper the measurement point is, the later the pressure rises, the earlier the maximum pressure appears, and the higher the maximum pressure is. For example, the pressure of point M5 is 5.68 times that of the ICW, at 0.17 ms. The maximum pressure of A2 is only 4.40 kPa, 2.10 times the ICW, which appears at 0.26 ms. It is interesting noting that the pressure of A1 and B1 first increases and then stabilizes at a pressure close to the ICW. A time lag of 0.015 ms can be observed on the pressure curve of A1 and B1. Harmonic-liked oscillations appear on the pressure curves of A2 and B2. Along the crack length direction, the pressure time histories of symmetrical points are identical. The pressure of M3 is the largest

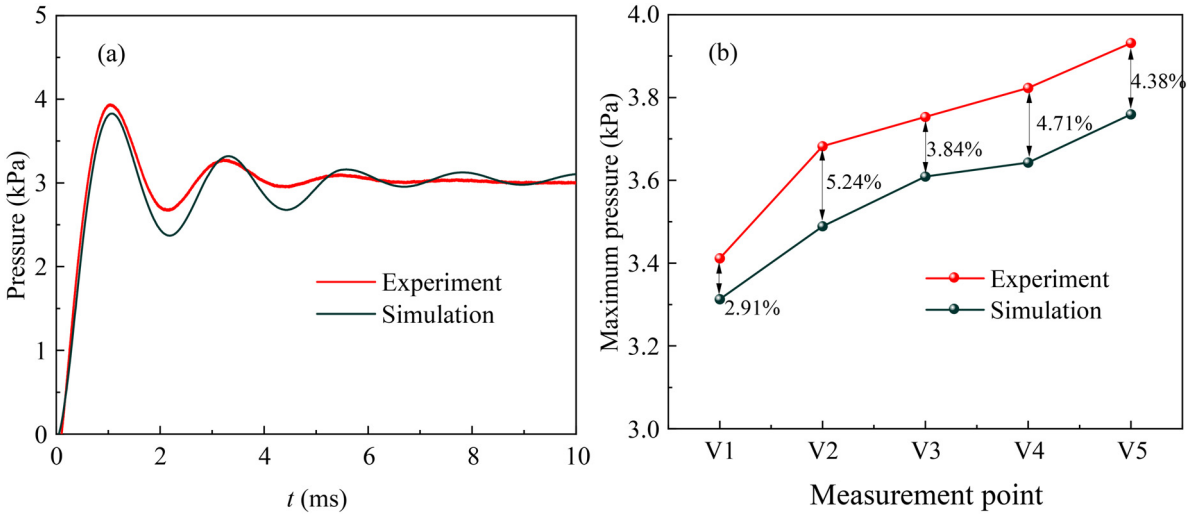

FIG. 14. Comparison of results: (a) pressure time histories and (b) maximum pressure.

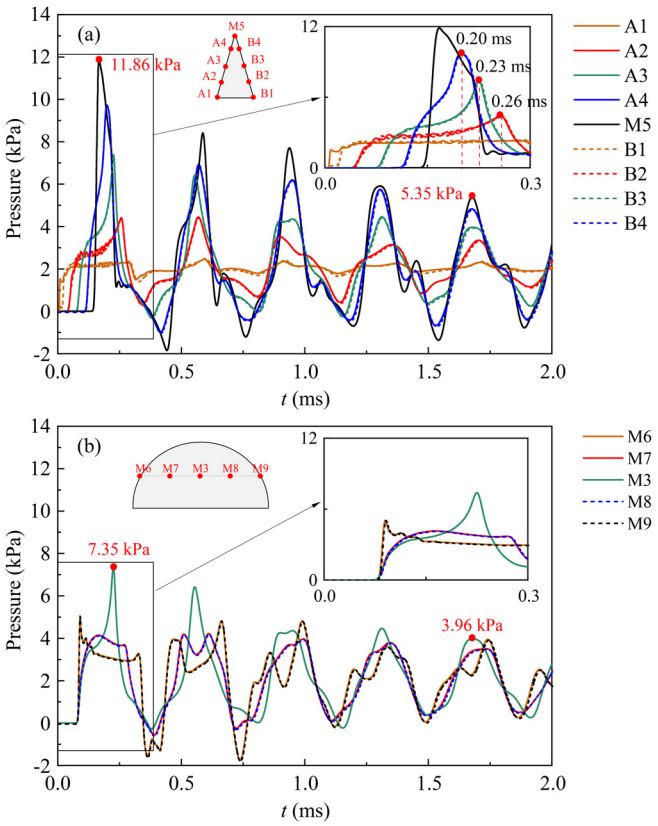

FIG. 15. Pressure time histories of the crack (*D*50-*W*5-*V*350): (a) crack depth direction and (b) crack length direction.

among all points in the crack length direction, whereas that of M6 is the least. The maximum pressure of M3 is 1.78 and 1.46 times that of M6 and M7.

B. Power spectrum density

To measure the aerodynamic power vs frequency, the power spectrum density (PSD) of the pressure time histories is calculated based on the fast Fourier transform (FFT). The PSD of all alternating components is plotted in 3D diagrams with double logarithmic axes. As shown in Fig. 16, the spectrum curve of all monitoring points first increases and then decreases in the frequency domain. Most of the aerodynamic impact energy, over 95%, belongs to a frequency range of 500–4000 Hz, a range of sonic frequency. The same dominant frequency of 2499 Hz can be observed on the PSD curves of all monitoring points. The PSD of the aerodynamic pressure increases with the depth. The PSD of monitoring point M5 is 1.18, 1.98, 5.75, and 91.04 times that of M4, M3, M2, and M1. Along the length direction, the PSDs of symmetry points are close when $f = 2499$ Hz. The value of monitoring point M3 is the highest, which is 19.2% and 100.0% higher than monitoring points M7 and M6.

The concept of proportion of PSD (PPSD) is introduced here to further reveal the characteristic of the aerodynamic impact energy. The PPSD is defined as the ratio of the PSD at a certain frequency to the sum of PSDs in the whole frequency domain. When $f = 0$ Hz, the PPSD describes the proportion of aerodynamic energy occupied by the average component of the pressure; when $f > 0$ Hz, the PPSD denotes the proportion of aerodynamic energy occupied by the fluctuating component.

Figure 17(a) shows the PPSD of monitoring point M5 when the frequency is lower than 4000 Hz. As shown in Fig. 17(a), the PPSD curve has two peaks at $f = 0$ and $f = 2499$ Hz, accounting for 65.6% and 9.3% of the sum of PSDs, respectively. This phenomenon indicates that most of the aerodynamic energy is occupied by the average component of the pressure wave. Figures 17(b) and 17(c) further present the PPSD when $f = 0$ and $f = 2499$ Hz to represent the proportion of aerodynamic energy occupied by the average and fluctuating component, respectively. As shown in Fig. 17(b), the deeper the monitoring point is, the stronger the aerodynamic impact of fluctuating components of the pressure wave is. The closer the monitoring points to the crack mouth, the more susceptible to the average component of the pressure wave. When $f = 0$ Hz, the PPSD of monitoring point M1 is 43.8% higher than that of M5. When $f = 2499$ Hz, the PPSD of monitoring point M1 is only 0.3%, whereas that of M5 reaches 9.3%. As illustrated in Fig. 17(c), along the crack length direction, the PPSD of different monitoring points is also symmetric. The PPSD of monitoring point M3 is the highest, reaching 87.1% and 3.4% when $f = 0$ and $f = 2499$ Hz, respectively.

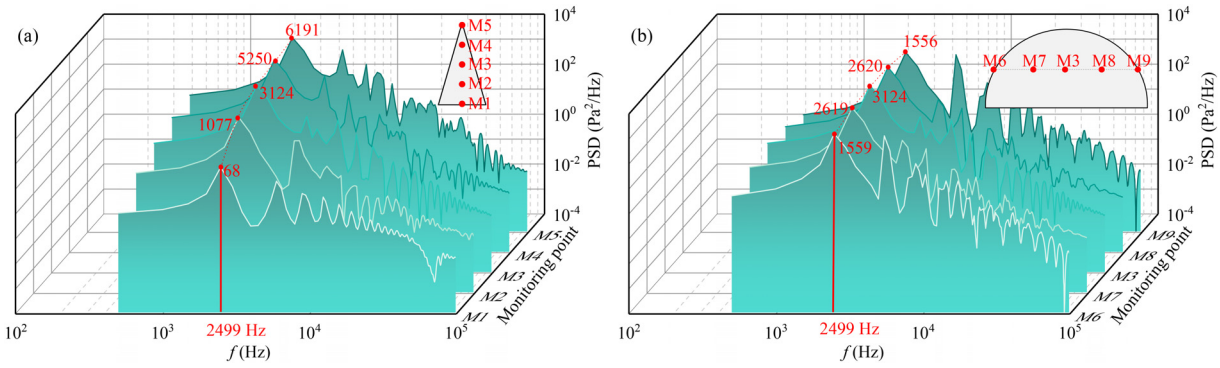

FIG. 16. Power spectrum density (*D*50-*W*5-*V*350): (a) crack depth direction and (b) crack length direction.

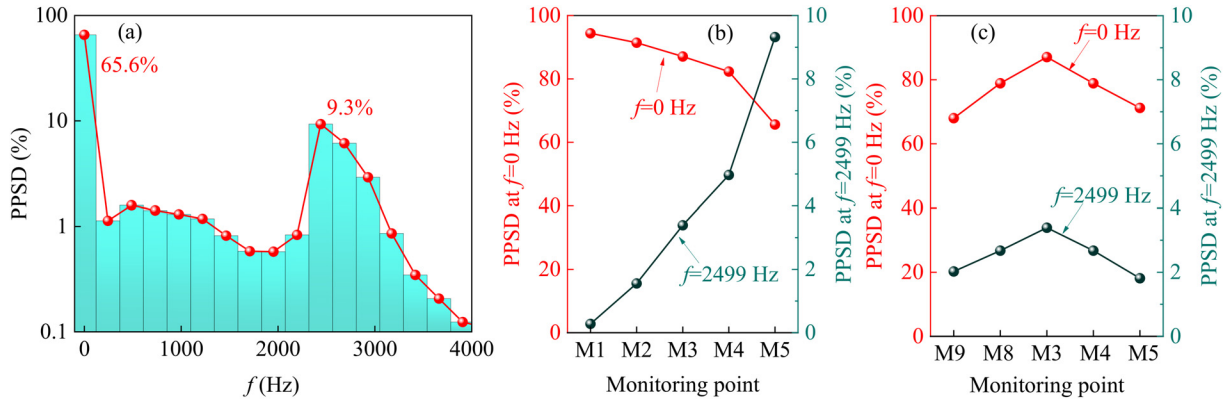

FIG. 17. PPSD (*D*50-*W*5-*V*350): (a) monitoring point M5 with the frequency of 0–4000 Hz; (b) crack depth direction; and (c) crack length direction.

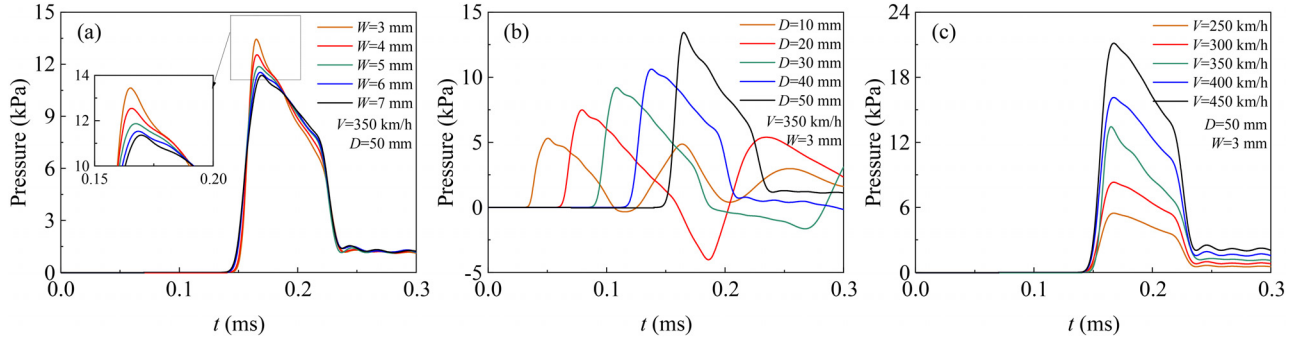

FIG. 18. Influential parameters of the pressure history: (a) crack width; (b) crack depth; and (c) train velocity.

V. INFLUENTIAL PARAMETERS ON AMPLIFIED PRESSURE

A. Pressure field

Figure 18 shows the influence of crack widths, crack depths, and train velocities on the pressure time history of M5. Figure 19 presents corresponding maximum pressures and fitting curves. For convenience, the linear function is used to fit the relationship of maximum pressures to crack widths and depths. The power function is recommended to evaluate the aerodynamic impact of train-induced pressures on structures.[28,32,33] Hence, the power function is adopted in Fig. 19(c).

As shown in Fig. 18, the shape of pressure time histories is insensitive to the change of different parameters. The maximum pressure increases with the increase in the crack depth and the train velocity, and decreases with the increase in the crack width. The decreasing

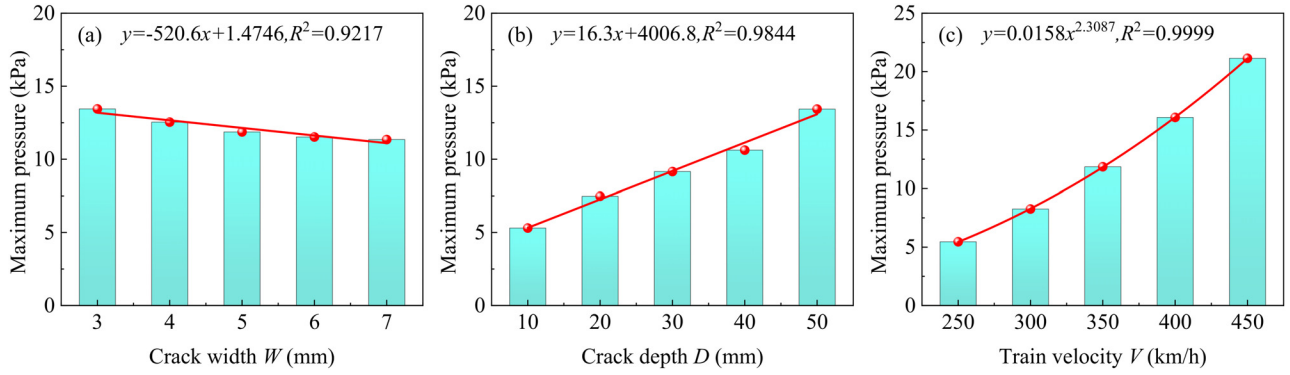

FIG. 19. Influential parameters of the maximum pressure: (a) crack width; (b) crack depth; and (c) train velocity.

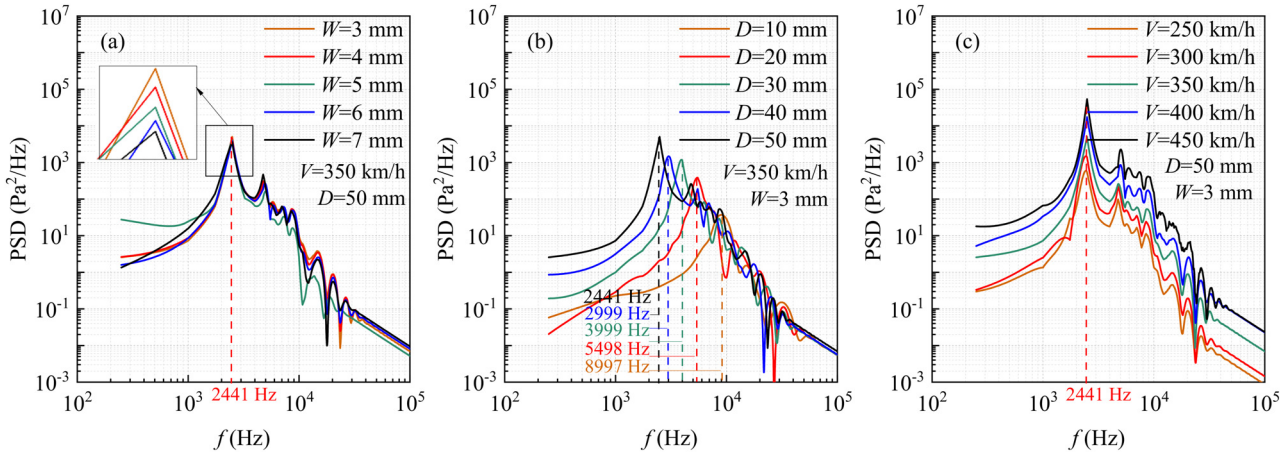

FIG. 20. Influential parameters of the PSD curve: (a) crack width; (b) crack depth; and (c) train velocity.

crack depth shortens the time of pressure oscillation. This is why three periods of pressure oscillations can be observed when $D = 10$ mm, whereas only one period for cracks with $D > 40$ mm within 0.3 ms. As shown in Fig. 19, the train velocity is the most influential parameter on the aerodynamic impact of the crack tip, followed by the crack depth. When the train velocity increases from 250 to 450 km/h, the maximum pressure increases by 387.5%; when the crack depth increases from 10 to 50 mm, the maximum pressure increases by 253.2%. However, the maximum pressure decreases by 15.5% when the crack width increases from 3 to 7 mm. The relationship of the maximum pressure to crack widths and depths can be well described by the linear function with slopes of −520.6 and 16.3, respectively. The power function with an exponent of 2.3087 is also applicable for evaluating the relationship between the maximum pressure and train velocities. It is worth mentioning that the train-induced aerodynamic pressure is normally proportional to the second power of the train velocity.[34,35] Hence, we may speculate that the train-induced aerodynamic impact on the crack tip is stronger than that on trackside structures.

B. Power spectrum density

Figure 20 shows the influence of crack widths, crack depths, and train velocities on the PSD of pressure time histories of M5. As can be seen in the figure, the shape of PSD curves under different conditions is also similar. The PSD of pressure time histories first increases and then decreases. All the PSD curves have a dominant frequency. The dominant frequency is insensitive to the change in crack width and train velocity, whereas it is sensitive to the change in crack depth. It is also found that the maximum PSD increase with the increase in the crack depth and train velocity, whereas decrease with the increase in the crack width. Figure 21 further presents the maximum PSD. As shown in Fig. 21, the power function is more reasonable to describe the relationship between the maximum PSD and the crack widths, crack depths, and train velocities. The train velocity and crack depth are also the most influential parameters to the maximum PSD. The maximum PSD decreases by 28.8% when the crack width increases from 3 to 7 mm.

According to the above analysis, the propagating time of the pressure wave along the crack depth direction contributes most to the dominant frequency. If a pressure wave incident into a crack along the crack depth direction, the dominant frequency of the aerodynamic pressure can be calculated according to [Eq. (1)]. However, when the propagation direction of the pressure wave is perpendicular to the crack depth direction, an acoustic length correction, represented by D_c, has to be made.[36] The corrected calculation formula is written as

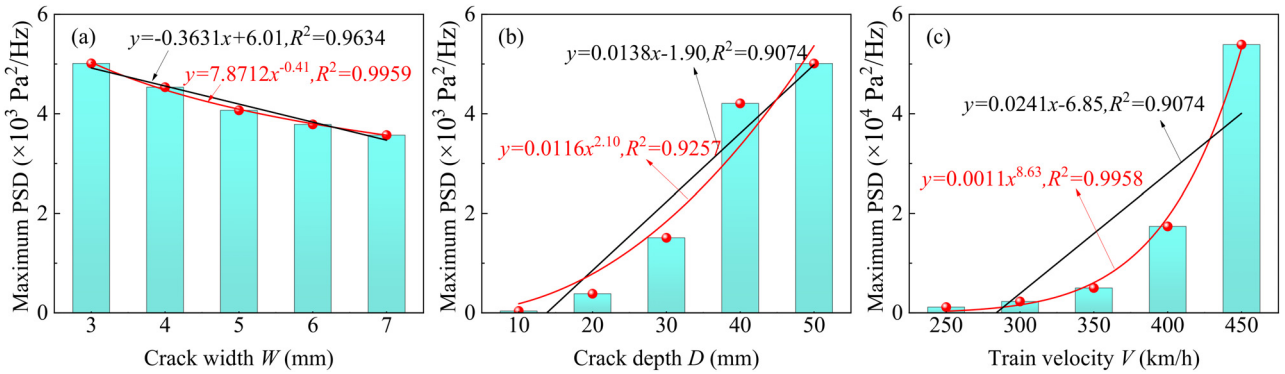

FIG. 21. Influential parameters of the maximum PSD: (a) crack width; (b) crack depth; and (c) train velocity.

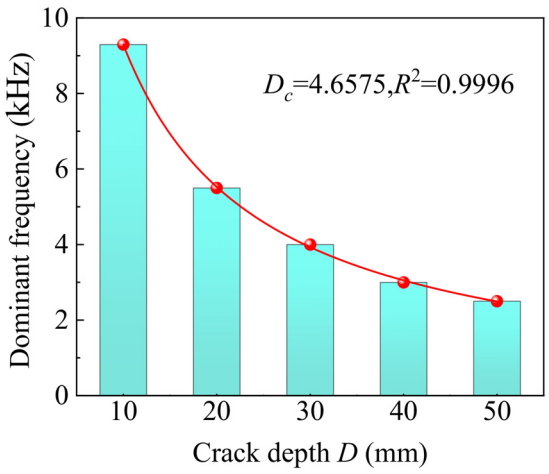

FIG. 22. Influence of crack depth on dominant frequency.

[Eq. (2)]. [Eq. (2)] is used to fit the relationship between the crack depth and the corresponding dominant frequency. As shown in Fig. 22, the determination coefficient is 0.9996 and the corresponding correction coefficient D_c is 4.6574, signaling that the proposed formula can be well used to predict the dominant frequency of the aerodynamic pressure inside lining cracks:

$$f_D = \frac{c}{2D}, \tag{1}$$

$$f_D = \frac{c}{2(D + D_c)}, \tag{2}$$

where f_D is the dominant frequency in Hz; c is the sound speed and $c = 340$ m/s; D is the crack depth in m; D_c is the correction coefficient of the crack depth.

Figure 23 shows the influence of crack widths, crack depths, and train velocities on the PPSD of pressure time histories of M5 at 0 Hz and the dominant frequency. As shown in Fig. 23, when $f = 0$ Hz, the crack depth is the most influential parameter on the PPSD, whereas the crack width and train velocity have limited influence. When the crack depth increases from 10 to 50 mm, the PPSD decreases from 93.8% to 45.8%. At the dominant frequency, the PPSD is most susceptible to the crack depth, followed by the crack width and the train velocity. When the crack width increases from 3 to 7 mm, the PPSD decreases from 9.9% to 6.8%; when the train velocity increases from 250 to 450 km/h, the PPSD increases from 7.9% to 11.9%. However, when the crack depth increases from 10 to 50 mm, the PPSD increases from 0.2% to 13.9%. As discussed above, the aerodynamic impact of the average component of pressure waves on the crack becomes more significant when the crack depth increases. The aerodynamic impact of the fluctuating component of pressure waves on the crack becomes more significant when the crack depth and the train velocity increase, and decreases when the crack width increases.

VI. MECHANISMS FOR PRESSURE WAVE INCIDENCE AND AMPLIFICATION

A. Pressure wave incidence and reflection

From the microscopic view, the increase in the number of air molecules per unit volume increases the sum of the speed of all air molecules, leading to an increased local wind speed. To reveal the mechanism of the pressure incidence, Fig. 24 shows the time histories of the wind speed of each monitoring point along the crack depth direction in *D*50-*W*5-*V*350. As shown in Fig. 24, the wind speed of A1 and B1 rises first. The wind speed increases orderly with the increase in the depth of monitoring points. The maximum wind speed monitored by A1 is 17.24 m/s at 0.03 ms, which is the maximum value among all monitoring points. Apart from A5, the wind speed of all monitoring points undergoes an up-down-up-down process. This is because the pressure wave propagates to the crack mouth direction after it reaches the crack tip. The maximum wind speed of A4, A3, and A2 is observed at $t = 0.20$, 0.23, and 0.26 ms. These moments are consistent with moments when the maximum pressure of each monitoring point appears, as shown in Fig. 15, signaling the rationality of using wind speed to explain the wave propagation.

Figure 25 presents the evolution of wind speed contours on the plane at *L*/2 in case *D*50-*W*5-*V*350. As illustrated in Fig. 25, the wave

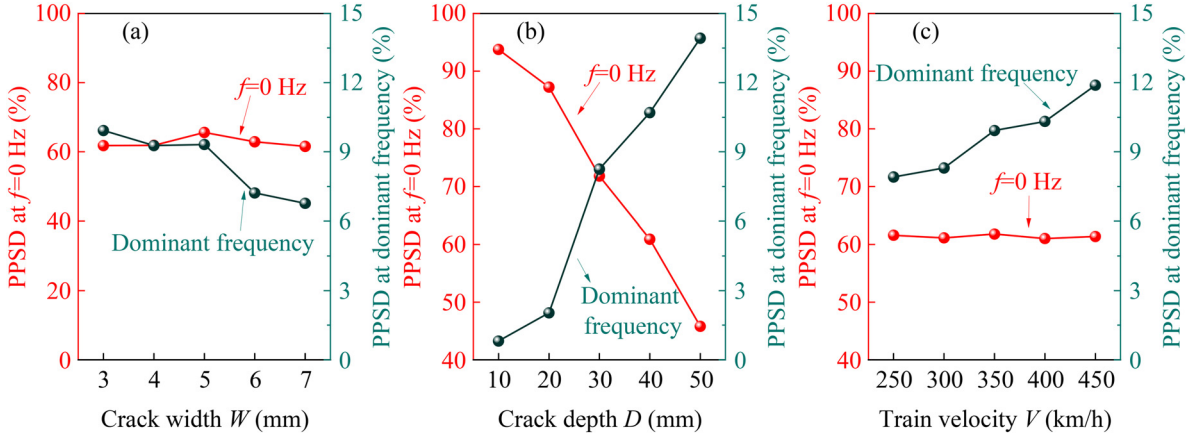

FIG. 23. Influential parameters of the PPSD: (a) crack width; (b) crack depth; and (c) train velocity.

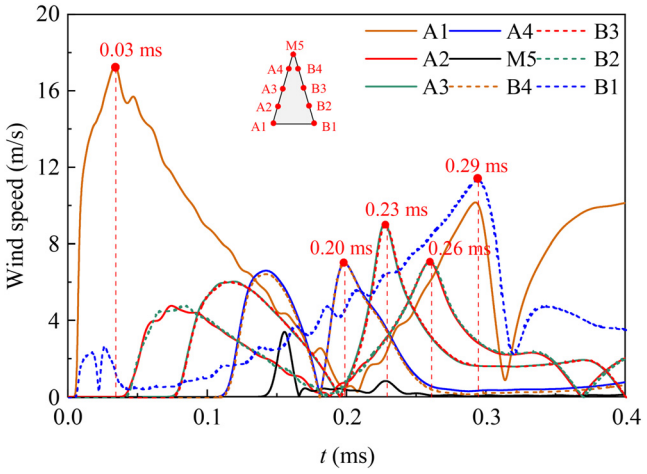

FIG. 24. Time histories of wind speed (*D*50-*W*5-*V*350).

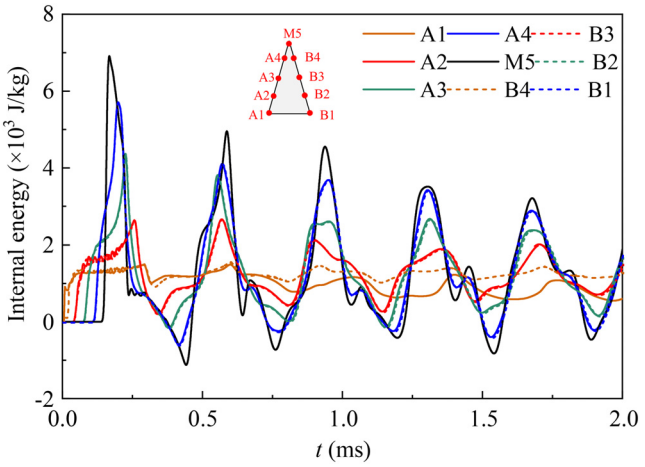

FIG. 26. Time history of internal energy of A5 in *D*50-*W*5-*V*350.

diffraction effect is the reason why the ICW incidents into the crack. According to the Huygens–Fresnel principle, all air molecules on a wavefront can be regarded as a point source for a secondary wave.[37,38] Before encountering the crack, the ICW propagates along the tunnel's longitudinal direction. The wave diffraction phenomenon happens when the ICW travels to the corner of the crack and the tunnel vault at 0.01 ms. The wind speed near the corner increases due to more air molecules being motivated by the ICW when the space for the wave enlarges at 0.02 ms. After that, the local area of high-wind speed continues to enlarge. This area acts as a new wave source to produce secondary waves propagating in all directions. At $t = 0.05$ ms, the wind speed near surface B starts to increase, indicating that the secondary pressure wave already propagates into the crack. Then, at approximately 0.06 ms, the secondary pressure wave reflects from surface B to A. The secondary pressure wave cannot transmit through a solid surface, causing the wave to reverse direction. Hence, the wave reflection happens inside the crack.

B. Pressure amplification

The increase in the number of air molecules per unit volume also increases the internal energy in the volume, inducing a rise in the pressure.[39] Figure 26 shows the time histories of internal energy of each monitoring point along the crack depth direction in *D*50-*W*5-*V*350. The air is compressed when the internal energy is positive, or the air is expended. As shown in Fig. 26, the internal energy is zero at the initial state. The internal energy curve presented in this figure well coincides with the pressure time history, indicating that the change of internal energy is the direct cause of pressure variation in our investigated cases.

To reveal the energy mechanism behind the pressure amplification, Figs. 27 and 28 present the contours of internal energy on the plane at *L*/2 and the middle plane between two crack surfaces in *D*50-*W*5-*V*350, respectively. The mechanism of pressure amplification in the circumferential crack is: First, the superposition of the internal energy possessed by air molecules near crack surfaces, and second, the increase in the internal energy of air near the crack tip because of the gradually narrowing space.

As shown in Fig. 27(a), after the pressure propagates into the crack (0.05 ms), air molecules near the crack mouth are activated. The internal energy near the crack mouth increases, leading to the pressure of A1 and B1 increases. We can clearly see that local areas of high internal energy exist near two crack surfaces at different moments. For

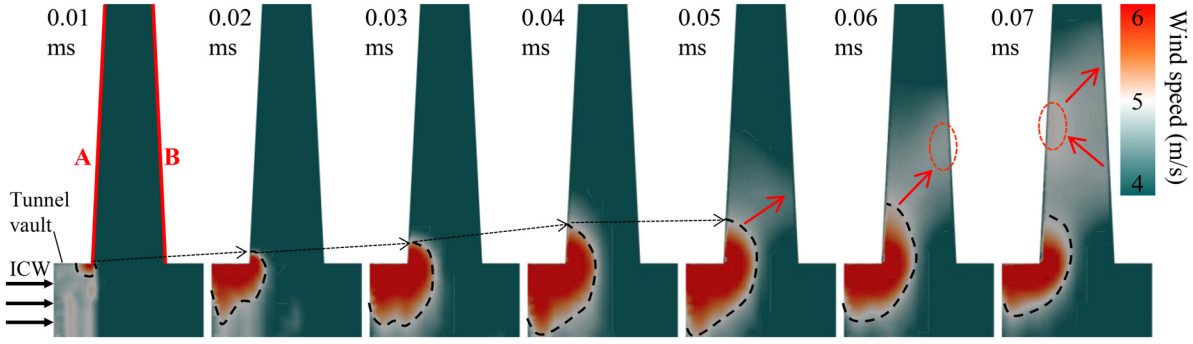

FIG. 25. The evolution of velocity contours on the plane at *L*/2 (*D*50-*W*5-*V*350).

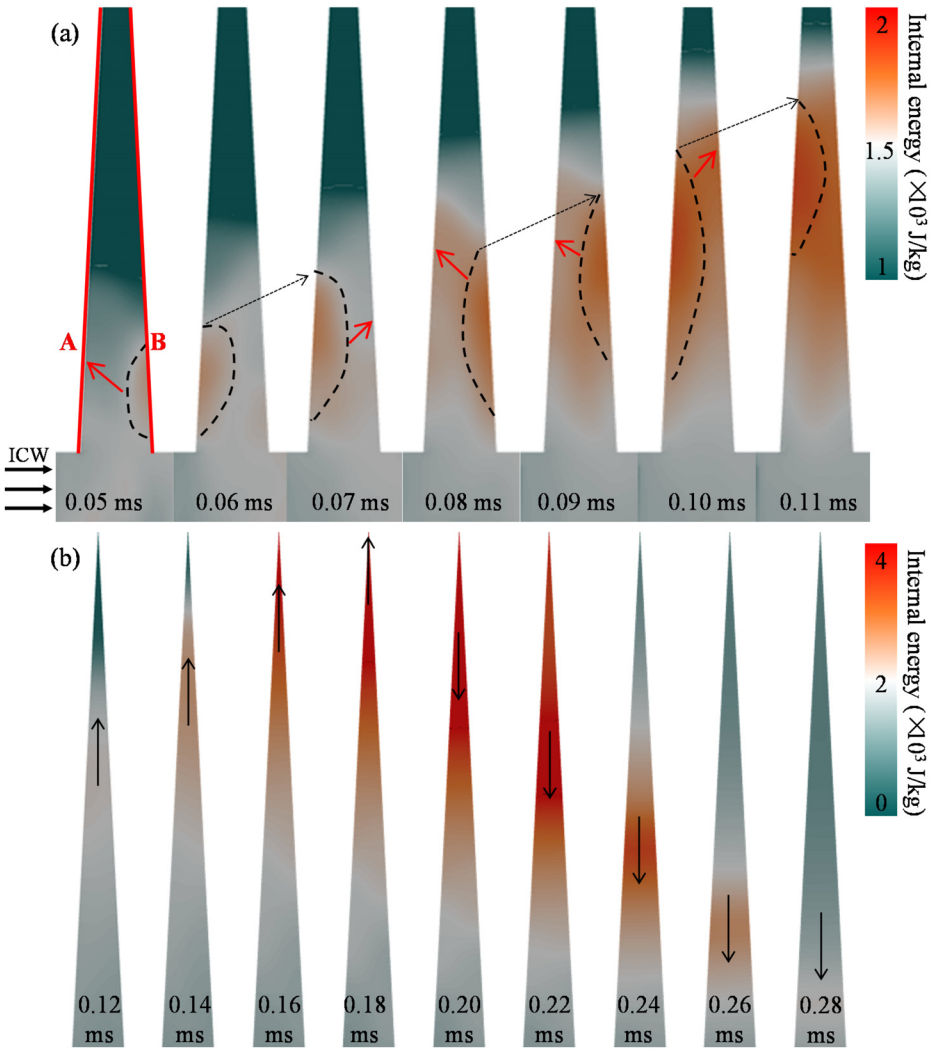

FIG. 27. Contours of internal energy on the plane at *L*/2 (*D*50-*W*5-*V*350): (a) pressure superposition before arriving at the crack tip and (b) pressure reflection at the crack tip.

example, at 0.05 ms, the local area with high internal energy exists near surface B. This is because the motion of air molecules is limited by surface B. The air molecules are reflected to surface A. The density of air molecules in this area increases, leading to higher internal energy. This is one of the main causes of the pressure superposition of the ICW. Furthermore, it is also seen that the internal energy increases with time, indicating that the pressure superposition strengthens whenever air molecules reflect. As shown in Fig. 27(b), from 0.12 to 0.18 ms, the space for air molecules narrows, and the internal energy increases, resulting in the pressure rising. The internal energy reaches the maximum value at the crack tip, leading to the maximum pressure at the crack tip. After that, the high-energy area moves toward the

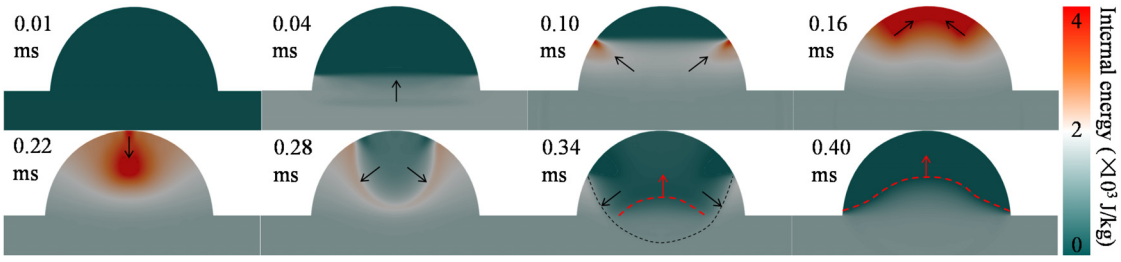

FIG. 28. Contours of internal energy on the middle plane between two crack surfaces (*D*50-*W*5-*V*350).

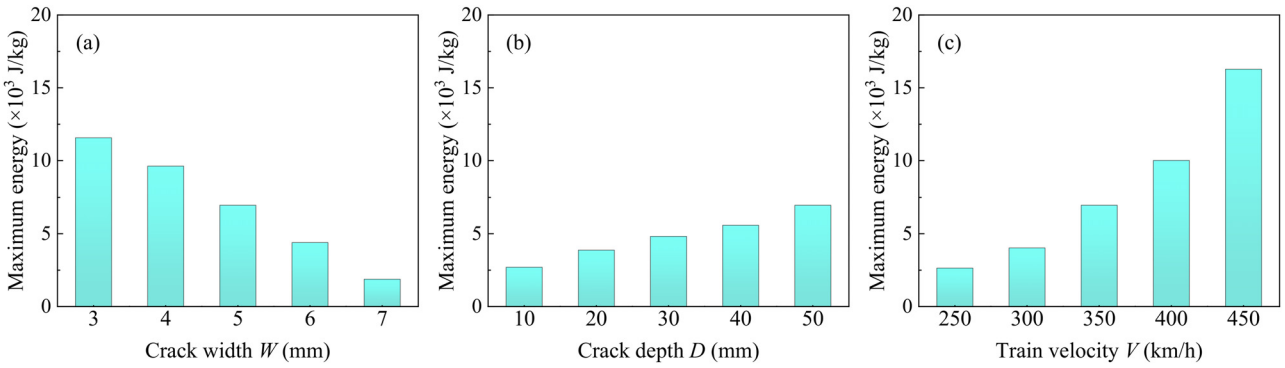

FIG. 29. Influential parameters of the maximum internal energy: (a) crack width; (b) crack depth; and (c) train velocity.

crack mouth. The pressure of each monitoring point maximizes when the high-energy area passes through. Meanwhile, the internal energy gradually decreases due to the space for air molecules expanding. This is the cause of the descending section of the pressure time history.

As shown in Fig. 28, during the incident process of the pressure wave, the internal energy is symmetrically distributed on the middle plane between two crack surfaces. This is why the pressure time histories of symmetry monitoring points are identical. Moreover, at 0.1 ms, the closer to the crack tip, the larger the internal energy is, causing the maximum pressure of M6 to be greater than that of M7. After 0.22 ms, the pressure wave moves downward, and the front of the internal energy is like an arc. After 0.34 ms, the pressure wave reflects at the crack mouth and propagates into the crack for the second time. The shape of the wavefront changes from a straight line (0.04 ms) to an arc. Therefore, the pressure of monitoring points increases for the second time and the pressure curve of each period is slightly different.

Figure 29 gives the maximum internal energy of M5 under different conditions. As shown in Fig. 29, the influence law of the three parameters on the internal energy is similar to those on the maximum pressure. The maximum internal energy decreases with the increase in the crack width and increases with the increase in the crack depth and the train velocity. The internal energy decreases by 616.4% when the crack width increases from 3 to 7 mm, and the value increases by 257.8% when the crack depth increases from 10 to 50 mm. The reason is that when the crack width increases and the crack depth decreases, the angle between two crack surfaces increases, so the internal energy of air at the crack tip increases, increasing the maximum pressure. It is also intuitively understood that the maximum pressure has a positive correlation with the train velocity because a higher train velocity brings higher input energy. The internal energy increases by 617.3% when the train velocity increases from 250 to 450 km/h.

VII. CONCLUSION

This study focuses on the aerodynamic amplification effect of the initial compression wave (ICW) in circumferential cracks in high-speed railway tunnels. The characteristics of amplified pressure, influential parameters, and corresponding mechanisms are analyzed and discussed in detail. The main conclusions are as follows:

(1) After ICW enters lining cracks, the pressure in cracks oscillates for approximately five periods with diminishing peaks and the shape of different periods is slightly different. The pressure in lining cracks is periodic waves with diminishing peaks. The pressure peak at the crack tip decreases from 11.86 to 5.35 kPa in five periods. Along the crack length direction, the pressure time histories of symmetrical points are identical. Along the crack depth direction, the deeper the measurement point is, the later the pressure rises, the earlier the maximum pressure appears, and the higher the maximum pressure is. For a typical case in real operation condition, the maximum pressure in a typical circumferential crack is 5.68 times that of the ICW.

(2) In a typical circumferential crack, the same dominant frequency of 2499 Hz can be observed on the power spectrum density (PSD) curves of all pressure time histories. When $f = 2499$ Hz, the PSD of the aerodynamic pressure at the crack tip is 91.04 times that at the crack mouth. The crack tip suffers most from the aerodynamic impact of the fluctuating component of pressure waves, whereas the crack mouth is most susceptible to the average component. When $f = 0$ Hz, the proportion of PSD (PPSD) of the crack tip is 43.8% higher than that of the crack mouth. When $f = 2499$ Hz, the PPSD of the crack mouth is only 0.3%, whereas that of the crack tip reaches 9.3%.

(3) The train velocity is the most influential parameter on the maximum pressure at the crack tip, followed by the crack depth. The maximum pressure increases with the increase in the crack depth and the train velocity, and decreases with the increase in the crack width. The relationship of the maximum pressure to crack widths and depths can be well described by the linear function with slopes of −520.6 and 19.4, respectively. The power function with an exponent of 2.3087 is applicable for evaluating the relationship between the maximum pressure and train velocities.

(4) The power function is more reasonable to describe the relationship between the maximum PSD and the crack widths, crack depths, and train velocities. The train velocity and crack depth are most influential parameters to the maximum PSD. A formula is proposed and well applied to predict the relationship between the crack depth and the corresponding dominant frequency. The aerodynamic impact of the average component of pressure waves on the crack becomes more significant when the crack depth increases. The aerodynamic impact of the fluctuating component of pressure waves on the crack becomes more significant when the crack depth and the train velocity increase,

and becomes less significant when the crack width increases. When the crack depth increases from 10 to 50 mm, the PPSD decreases from 93.8% to 45.8% when $f = 0$ Hz and increases from 0.2% to 13.9% at the dominant frequency.

(5) The mechanism of the incidence of the ICW is the wave diffraction effect. The wind speed near the corner of the crack and the tunnel vault increases due to more air molecules being motivated by the ICW. Then, this area acts as a new wave source to produce secondary waves propagating in all directions. The mechanism of pressure amplification in the circumferential crack is: First, the superposition of the internal energy possessed by air molecules near crack surfaces. Second, the increase in the internal energy of air near the crack tip is caused by gradually narrowing space.

In this research, the crack is idealized as two smooth surfaces and the two crack surfaces are simplified as semi-ellipses. In practice, the crack surfaces are rough and the shape is irregular, which affects the pressure wave propagation and amplification. The roughness and irregular shape of tunnel lining cracks will be considered in our future research.

ACKNOWLEDGMENTS

This work is funded by the National Natural Science Foundation of China (Grant Nos. 51978670 and U1934209); the Research Grants Council, University Grants Committee of the Hong Kong Special Administrative Region (SAR), China (Grant No. R-5020–18); the Innovation and Technology Commission of the Hong Kong SAR Government (Grant No. K-BBY1); The Hong Kong Polytechnic University's Postdoc Matching Fund Scheme (Grant No. 1-W21Q); and the Guangdong Basic and Applied Basic Research Foundation of Department of Science and Technology of Guangdong Province (Grant No. 2021B1515130006).

AUTHOR DECLARATIONS

Conflict of Interest

The authors have no conflicts to disclose.

Author Contributions

Yi-Kang Liu: Investigation (lead); Software (lead); Writing – original draft (lead); Writing – review & editing (equal). **Wei-Chao Yang:** Conceptualization (lead); Funding acquisition (lead); Project administration (lead). **E. Deng:** Data curation (lead); Funding acquisition (equal); Methodology (lead); Supervision (lead); Writing – review & editing (lead). **Zheng-Wei Chen:** Resources (equal); Writing – review & editing (equal). **Yi-Qing Ni:** Resources (equal); Writing – review & editing (equal).

DATA AVAILABILITY

The data that support the findings of this study are available from the corresponding author upon reasonable request.

REFERENCES

[1]C. H. Shi, A. Wang, X. H. Sun, and W. C. Yang, "Aerodynamic behavior and impact on driving safety of spalling blocks comprising high-speed-railway tunnel lining," Appl. Sci. **12**(5), 2593 (2022).
[2]C. H. Shi, A. Wang, X. H. Sun, and W. C. Yang, "Research on the movement law and traffic safety zoning of spalled blocks in the linings of high-speed railway tunnels," Tunnelling Underground Space Technol. **128**, 104614 (2022).
[3]T. Asakura and Y. Kojima, "Tunnel maintenance in Japan," Tunnelling Underground Space Technol. **18**(2–3), 161 (2003).
[4]H. Q. Bi, Z. H. Wang, H. L. Wang, and Y. L. Zhou, "Aerodynamic phenomena and drag of a maglev train running dynamically in a vacuum tube," Phys. Fluids **34**(9), 096111 (2022).
[5]J. Y. Kim and K. Y. Kim, "Experimental and numerical analyses of train-induced unsteady tunnel flow in subway," Tunnelling Underground Space Technol. **22**(2), 166 (2007).
[6]P. R. Murray and M. S. Howe, "Influence of hood geometry on the compression wave generated by a high-speed train," J. Sound Vib. **329**(14), 2915 (2010).
[7]Y. B. Chen, Y. Gao, S. H. Shi, F. Xu, and W. G. Zhao, "Characteristics of transient pressure in lining cracks induced by high-speed trains," J. Wind Eng. Ind. Aerodyn. **228**, 105120 (2022).
[8]N. Zhang, X. J. Zhu, and Y. F. Ren, "Analysis and study on crack characteristics of highway tunnel lining," Civ. Eng. J. **5**(5), 1119 (2019).
[9]R. D. Xue, X. H. Xiong, X. B. Li, and G. Chen, "Influence of turbulent incoming flow on aerodynamic behaviors of train at 90 degrees yaw angle," Phys. Fluids **35**(1), 015121 (2023).
[10]S. Zhong, M. Z. Yang, B. Qian, T. T. Wang, F. Wu, and L. Zhang, "Temporal evolution of flow field structure for vehicles accelerating in evacuated tube transportation system," Phys. Fluids **35**(2), 025117 (2023).
[11]A. Baron, P. Molteni, and L. Vigevano, "High-speed trains: Prediction of micro-pressure wave radiation from tunnel portals," J. Sound Vib. **296**(1–2), 59 (2006).
[12]L. Zhang, M. Z. Yang, X. F. Liang, and J. Zhang, "Oblique tunnel portal effects on train and tunnel aerodynamics based on moving model tests," J. Wind Eng. Ind. Aerodyn. **167**, 128 (2017).
[13]H. Okubo, T. Miyachi, and K. Sugiyama, "Pressure fluctuation and a micro-pressure wave in a high-speed railway tunnel with large branch shaft," J. Wind Eng. Ind. Aerodyn. **217**, 104751 (2021).
[14]H. Okubo, T. Miyachi, and T. Fukuda, "Field test for micro-pressure wave reduction measurement by area optimization of windows of tunnel hoods," Proc. Inst. Mech. Eng., Part F **236**(10), 1262 (2022).
[15]H. Q. Tian, "Review of research on high-speed railway aerodynamics in China," Transp. Saf. Environ. **1**(1), 1–21 (2019).
[16]T. T. Wang, Y. Zhu, X. D. Tian, F. C. Shi, L. Zhang, and Y. B. Lu, "Design method of the variable cross-section tunnel focused on improving passenger pressure comfort of trains intersecting in the tunnel," Build. Environ. **221**, 109336 (2022).
[17]T. H. Liu, Z. W. Chen, X. D. Chen, T. Z. Xie, and J. Zhang, "Transient loads and their influence on the dynamic responses of trains in a tunnel," Tunnelling Underground Space Technol. **66**, 121 (2017).
[18]W. Zhou, L. Chen, Z. G. Wang, S. S. Ding, and Y. L. Shan, "Aerodynamic load spectrum and fatigue behaviour of high-speed train's equipment cabin," Fatigue Fract. Eng. Mater. Struct. **42**(11), 2579 (2019).
[19]C. Gong and Z. D. Zhu, "Numerical study for the aerodynamic effects of high-speed trains on secondary lining," Henan Sci. **36**(5), 721 (2018) (in Chinese), see https://kns.cnki.net/kcms/detail/41.1084.N.20180605.1656.034.html
[20]J. M. Du, Q. Fang, G. Wang, D. L. Zhang, and T. L. Chen, "Fatigue damage and residual life of secondary lining of high-speed railway tunnel under aerodynamic pressure wave," Tunnelling Underground Space Technol. **111**, 103851 (2021).
[21]F. L. Li, J. J. Luo, L. Wang, D. K. Wang, and L. P. Gao, "Wave effects of high-speed trains passing through different tunnel lining types," J. Wind Eng. Ind. Aerodyn. **224**, 104971 (2022).
[22]F. Y. Wang, M. L. Zhou, D. M. Zhang, H. W. Huang, and D. Chapman, "Random evolution of multiple cracks and associated mechanical behaviors of segmental tunnel linings using a multiscale modeling method," Tunnelling Underground Space Technol. **90**, 220 (2019).
[23]L. Xu and M. Ma, "Study of the characteristics of train-induced dynamic SIFs of tunnel lining cracks based on the modal superposition approach," Eng. Fract. Mech. **233**, 107069 (2020).
[24]Q. Feng, K. Sun, H. P. Chen, and X. Lei, "Long-term prediction of fatigue crack growth in ballastless track of high-speed railway due to cyclic train load," Constr. Build. Mater. **292**, 123375 (2021).

[25]W. H. Li, T. H. Liu, Z. W. Chen, Z. J. Guo, and X. S. Huo, "Comparative study on the unsteady slipstream induced by a single train and two trains passing each other in a tunnel," J. Wind Eng. Ind. Aerodyn. **198**, 104095 (2020).
[26]J. Q. Niu, D. Zhou, X. F. Liang, S. Liu, and T. H. Liu, "Numerical simulation of the Reynolds number effect on the aerodynamic pressure in tunnels," J. Wind Eng. Ind. Aerodyn. **173**, 187 (2018).
[27]P. Ricco, A. Baron, and P. Molteni, "Nature of pressure waves induced by a high-speed train travelling through a tunnel," J. Wind Eng. Ind. Aerodyn. **95**(8), 781 (2007).
[28]Y. K. Liu, W. C. Yang, E. Deng, Y. W. Wang, X. H. He, Y. M. Huang, and Z. W. Chen, "Aerodynamic impacts of high-speed trains on city-oriented noise barriers: A moving model experiment," Alexandria Eng. J. **68**, 343 (2023).
[29]H. L. Wang, B. Lei, H. Q. Bi, and T. Yu, "Wavefront evolution of compression waves propagating in high speed railway tunnels," J. Sound Vib. **431**, 105 (2018).
[30]China State Railway Group Co. LTD, *Assessment Standard for Structure Deterioration of Railway Bridge and Tunnel–Part 2: Tunnel* (China State Railway Group Co. LTD, 2019).
[31]C. Huang, T. Chen, Z. Xia, and L. Jiang, "Numerical study of surface fatigue crack growth in steel plates repaired with CFRP," Eng. Struct. **268**, 114743 (2022).
[32]X. H. Xiong, A. H. Li, X. F. Liang, and J. Zhang, "Field study on high-speed train induced fluctuating pressure on a bridge noise barrier," J. Wind Eng. Ind. Aerodyn. **177**, 157 (2018).
[33]W. C. Yang, D. H. Ouyang, E. Deng, Y. W. Wang, Z. W. Chen, X. H. He, and Y. M. Wang, "Deterioration of aerodynamic performance of a train driving through noise barriers under crosswinds," J. Wind Eng. Ind. Aerodyn. **231**, 105241 (2022).
[34]M. Tokunaga, M. Sogabe, T. Santo, and K. Ono, "Dynamic response evaluation of tall noise barrier on high speed railway structures," J. Sound Vib. **366**, 293 (2016).
[35]D. Zhou, H. Q. Tian, J. Zhang, and M. Z. Yang, "Pressure transients induced by a high-speed train passing through a station," J. Wind Eng. Ind. Aerodyn. **135**, 1–9 (2014).
[36]Z. L. Ji, "Acoustic length correction of closed cylindrical side-branched tube," J. Sound Vib. **283**(3–5), 1180 (2005).
[37]Z. Q. Cao, C. White, and K. Kontis, "Numerical investigation of rarefied vortex loop formation due to shock wave diffraction with the use of rorticity," Phys. Fluids **33**(6), 067112 (2021).
[38]T. S. Rappaport, *Wireless Communications: Principles and Practice*, 2nd ed. (Pearson Education, India, 2010).
[39]P. X. Guo, F. C. Shi, Z. X. Gao, C. W. Jiang, C. H. Lee, and C. Wen, "Heat transfer and behavior of the Reynolds stress in Mach 6 boundary layer transition induced by first-mode oblique waves," Phys. Fluids **34**(10), 104116 (2022).